ATLAS NOTE

ATLAS-CONF-2014-024

May 19, 2014

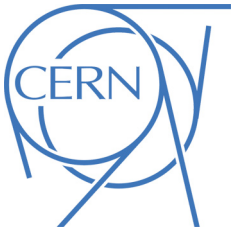

Centrality and rapidity dependence of inclusive jet production in $\sqrt{s_{\mathrm{NN}}} = 5.02$ TeV proton–lead collisions with the ATLAS detector

The ATLAS Collaboration

Abstract

The ATLAS Collaboration has measured the centrality and rapidity dependence of inclusive jet production in $\sqrt{s_{\mathrm{NN}}} = 5.02$ TeV proton–lead (p+Pb) collisions and the jet cross-section in $\sqrt{s} = 2.76$ TeV proton-proton collisions in datasets corresponding to an integrated luminosity of 27.8 nb^{-1} and 4.0 pb^{-1}, respectively, recorded at the Large Hadron Collider in 2013. The p+Pb collision centrality was characterised using the total transverse energy measured in the pseudorapidity interval $3.2 < \eta < 4.9$ in the direction of the lead beam. Jets were reconstructed using the anti-k_t algorithm with $R = 0.4$ from energy deposits measured in the ATLAS calorimeter. Results are presented for the double differential per-collision yields as a function of jet rapidity and transverse momentum for both minimum bias and centrality-selected p+Pb collisions. The central-to-peripheral ratio R_{CP} and the nuclear modification factor R_{pPb} are evaluated to probe deviations in the jet rate from the geometric expectation. The total yield of jets in minimum bias p+Pb collisions is consistent with a small p_{T}-dependent excess above the expectation. The ratios of jet spectra between different centrality selections, corrected for the corresponding partonic luminosities, show a centrality-dependent modification of jet production at all p_{T} at forward rapidities and at large p_{T} at mid-rapidity. When compared to the expectation from independent nucleon-nucleon collisions, this modification appears as a suppression of jets in central events and an enhancement in peripheral events. These effects imply that the factorisation between hard and soft processes is violated at an unexpected level in proton-nucleus collisions. Furthermore, the violations may have a simple dependence on the hard parton-parton kinematics.

ATLAS-CONF-2014-024
20 May 2014

1 Introduction

Proton–lead (p+Pb) collisions at the Large Hadron Collider (LHC) provide a unique opportunity to study hard scattering processes involving a nuclear target [1]. Measurements of jets in p+Pb collisions provide a valuable benchmark for studies of jet quenching in lead-lead collisions by, for example, constraining the impact of nuclear parton distributions on inclusive jet yields. However, p+Pb collisions also allow for the study of possible violations of the factorisation between hard and soft processes in collisions involving nuclei.

Previous studies in deuteron-gold (d+Au) collisions at RHIC showed such violations, manifested in the suppressed production of very forward hadrons with transverse momenta up to 4 GeV [2, 3, 4]. Studies of forward di-hadron angular correlations at RHIC also showed a much weaker dijet signal in d+Au collisions than in pp collisions [4, 5]. These effects have been attributed to the saturation of the parton distributions in the gold nucleus [6, 7, 8], to the modification of the parton distribution function in nuclei [9], to the higher-twist contributions to the cross-section enhanced by the forward kinematics of the measurement [10] or to the presence of a large nucleus [11]. The extended kinematic reach of p+Pb measurements at the LHC allows the study of hard scattering processes that produce forward hadrons or jets over a much wider rapidity and transverse momentum (p_{T}) range. Such measurements can determine whether the factorisation violations observed at RHIC persist at higher energy and, if so, how the resulting modifications vary as a function of particle or jet p_{T}. The results of such measurements could test the competing descriptions of the RHIC results, and, more generally, provide new insight into the physics of hard scattering processes involving a nuclear target.

This note reports the centrality dependence of high-p_{T} jet production in p+Pb collisions at a nucleon-nucleon centre-of-mass energy $\sqrt{s_{\mathrm{NN}}} = 5.02$ TeV. The measurement was performed using a data set corresponding to an integrated luminosity of 27.8 nb^{-1} recorded in 2013. The p+Pb jet yields were compared to a nucleon-nucleon reference constructed from a measurement of jet production in pp collisions at a centre-of-mass energy $\sqrt{s} = 2.76$ TeV using a data set corresponding to an integrated luminosity of 4.0 pb^{-1} also recorded in 2013. Jets were reconstructed using the anti-k_t algorithm with $R = 0.4$ [12] from energy deposits measured in the ATLAS calorimeter.

The centrality of p+Pb collisions was characterised using the total transverse energy measured in the pseudorapidity[1] interval $3.2 < \eta < 4.9$ in the direction of the lead beam. Whereas in nucleus-nucleus collisions centrality reflects the degree of nuclear overlap between the colliding nuclei, centrality in p+Pb collisions is sensitive to the multiple interactions between the proton and nucleons in the lead nucleus. Centrality has been successfully used at lower energies in d+Au collisions at RHIC as an experimental handle on the collision geometry [13, 14].

A Glauber model [15] was used to determine the average number of nucleon-nucleon collisions, $\langle N_{\mathrm{coll}} \rangle$, and the mean value of the overlap function, $T_{\mathrm{pA}}(b) = \int_{-\infty}^{+\infty} \rho(b,z)\mathrm{d}z$ in each centrality interval, where $\rho(b,z)$ is the nucleon density at impact parameter b and longitudinal position z. Per-event jet yields, $(1/N_{\mathrm{evt}})(\mathrm{d}^2N_{\mathrm{jet}}/\mathrm{d}p_{\mathrm{T}}dy^*)$, were measured as a function of jet centre-of-mass rapidity[2] y^* and transverse momentum p_{T}, where N_{evt} is the number of p+Pb events analyzed. The centrality dependence of the per-event jet yields was evaluated using the nuclear modification factor,

$$R_{\mathrm{pPb}} \equiv \frac{1}{T_{\mathrm{pA}}} \frac{(1/N_{\mathrm{evt}})\ \mathrm{d}^2N_{\mathrm{jet}}/\mathrm{d}p_{\mathrm{T}}dy^*\big|_{\mathrm{cent}}}{\mathrm{d}^2\sigma^{pp}_{\mathrm{jet}}/\mathrm{d}p_{\mathrm{T}}dy^*}, \tag{1}$$

[1] ATLAS uses a right-handed coordinate system with its origin at the nominal interaction point (IP) in the centre of the detector and the z-axis along the beam pipe. The x-axis points from the IP to the centre of the LHC ring, and the y-axis points upward. Cylindrical coordinates (r,ϕ) are used in the transverse plane, ϕ being the azimuthal angle around the beam pipe. The pseudorapidity is defined in laboratory coordinates in terms of the polar angle θ as $\eta = -\ln\tan(\theta/2)$.

[2] The jet rapidity y^* is defined as $y^* = 0.5 \ln \frac{E+p_z}{E-p_z}$ where E and p_z are the energy and the component of the momentum along the beam direction in the nucleon-nucleon centre-of-mass frame.

where $\mathrm{d}^2\sigma^{pp}_{\mathrm{jet}}/\mathrm{d}p_{\mathrm{T}}dy^*$ is determined using the jet cross-section measured at $\sqrt{s} = 2.76$ TeV. The R_{pPb} quantifies the absolute modification in the jet rate relative to the geometric expectation. In each centrality, the geometric expectation is the jet rate that would be produced by an incoherent superposition of a number of nucleon-nucleon collisions corresponding to the mean nuclear thickness in the selected class of p+Pb collisions.

Results are also presented for the central-to-peripheral ratio,

$$R_{\mathrm{CP}} \equiv \frac{1}{R_{\mathrm{coll}}} \frac{1/N_{\mathrm{evt}}\ \mathrm{d}^2N_{\mathrm{jet}}/\mathrm{d}p_{\mathrm{T}}dy^*\big|_{\mathrm{cent}}}{1/N_{\mathrm{evt}}\ \mathrm{d}^2N_{\mathrm{jet}}/\mathrm{d}p_{\mathrm{T}}dy^*\big|_{\mathrm{peri}}}, \tag{2}$$

where R_{coll} represents the ratio of the $\langle N_{\mathrm{coll}}\rangle$ in a given centrality interval to that in the most peripheral interval, $R_{\mathrm{coll}} \equiv \left\langle N^{\mathrm{cent}}_{\mathrm{coll}}\right\rangle / \left\langle N^{\mathrm{peri}}_{\mathrm{coll}}\right\rangle$. The R_{CP} is sensitive to deviations in the jet rate from the geometric expectation between the p+Pb event centralities. The R_{pPb} and R_{CP} measurements are presented as a function of the jet y^* and p_{T}.

For the 2013 p+Pb run, the LHC was configured with a 4 TeV proton beam and a 1.57 TeV per-nucleon Pb beam that together produced collisions with $\sqrt{s_{\mathrm{NN}}} = 5.02$ TeV and a rapidity shift of -0.465 or $+0.465$ relative to the ATLAS rest frame, depending on the run period. The run was split into two periods, with the directions of the proton and lead beams being reversed at the end of the first period. The first period provided approximately 55% of the integrated luminosity with the Pb beam travelling to positive rapidity and the proton beam to negative rapidity, and the remainder with the beams reversed. The analysis in this note uses the events from both periods of data-taking and y^* is defined so that $y^* > 0$ always refers to the downstream proton direction.

2 Experimental setup

The measurements presented in this note are performed using the ATLAS calorimeters, inner detector (ID), minimum-bias trigger scintillators (MBTS), and trigger and data acquisition systems [16]. The ID measures charged particles within $|\eta| < 2.5$ using a combination of silicon pixel detectors, silicon micro-strip detectors, and a straw-tube transition radiation tracker, all immersed in a 2 T axial magnetic field [17]. The calorimeter system consists of a liquid argon (LAr) electromagnetic (EM) calorimeter covering $|\eta| < 3.2$, a steel-scintillator sampling hadronic calorimeter covering $|\eta| < 1.7$, a LAr hadronic calorimeter covering $1.5 < |\eta| < 3.2$, and two LAr electromagnetic and hadronic forward calorimeters (FCal) covering $3.2 < |\eta| < 4.9$. The EM calorimeters are longitudinally segmented into three compartments with an additional pre-sampler layer in front for $|\eta| < 1.8$. The EM calorimeter has a granularity that varies with layer and pseudorapidity. The middle sampling layer, which typically has the largest energy deposit in EM showers, has a $\Delta\eta \times \Delta\phi$ granularity of 0.025×0.025 within $|\eta| < 2.5$. The hadronic calorimeter has three longitudinal segments with cell sizes $\Delta\eta \times \Delta\phi = 0.1 \times 0.1$ for $|\eta| < 2.5$ and 0.2×0.2 for $2.5 < |\eta| < 4.9$.[3]. The two radial FCal modules are composed of tungsten and copper absorbers with liquid argon as the active medium, which together provide 10 interaction lengths of material. The MBTS detects charged particles over $2.1 < |\eta| < 3.9$ using two hodoscopes of 16 counters positioned at $z = \pm 3.6$ m.

The p+Pb and pp events used in this analysis were recorded using a combination of minimum-bias (MB) and jet triggers [18]. In p+Pb, the minimum-bias trigger required hits in at least one counter in each side of the MBTS detector while in pp collisions the MB condition was the presence of hits in the pixel and strip detectors. Jets were selected using high-level jet triggers implemented with a reconstruction algorithm similar to that applied in the offline analysis. The high-level jet triggers were seeded from a combination of low level minimum-bias and jet hardware triggers. Multiple jet trigger thresholds ranging

[3] An exception is the third (outermost) sampling layer, which has a segmentation of 0.2×0.1 up to $|\eta| = 1.7$.

from 20 GeV to 75 GeV were used with pre-scales that varied with time to accommodate the evolution of the luminosity within an LHC fill.

3 Data selection

In the offline analysis, charged particle tracks were reconstructed in the ID using an algorithm optimised for pp minimum-bias measurements [19]. The p+Pb events used for this analysis were required to have a reconstructed vertex containing at least two associated tracks with $p_{\mathrm{T}} > 0.1$ GeV, at least one hit in each of the two MBTS hodoscopes, and a difference between times measured on the two MBTS sides of less than 10 ns. Events containing multiple p+Pb collisions (pileup) were suppressed by rejecting events having two or more reconstructed vertices, each associated with $\Sigma p_{\mathrm{T}} > 5$ GeV of reconstructed tracks. Events with a pseudorapidity gap (defined by the absence of energy clusters in the calorimeter with $E_{\mathrm{T}} > 0.2$ GeV) of greater than two units on the Pb-going side of the detector were also removed from the analysis. Such events arise primarily from electromagnetic or diffractive excitation of the proton. After accounting for event selection, the number of p+Pb events sampled by the highest-threshold jet trigger (which was unprescaled) was 53 billion.

The pp events used in this analysis were required to have a reconstructed vertex; no other requirements were applied.

4 Centrality determination

The centrality of the p+Pb events selected for analysis was characterised by the total transverse energy in the Pb-going FCal, $\Sigma E_{\mathrm{T}}^{\mathrm{Pb}}$. The $\Sigma E_{\mathrm{T}}^{\mathrm{Pb}}$ distribution for minimum-bias p+Pb collisions passing the above-described event selection is presented in Fig. 1. Following standard techniques [20], centrality intervals were defined in terms of percentiles of the $\Sigma E_{\mathrm{T}}^{\mathrm{Pb}}$ distribution after accounting for an estimated inefficiency of $2 \pm 2\%$ for inelastic p+Pb collisions to pass the applied event selections. The following centrality intervals were used in this analysis, in order from the most central to the most peripheral: 0–10%, 10–20%, 20–30%, 30–40%, 40–60%, 60–90%, with the 60-90% interval serving as the reference in the R_{CP}.

A Glauber Monte Carlo (MC) [15] analysis was used to calculate R_{coll} and T_{pA} for each of the centrality intervals. First, a Glauber MC program [21] was used to simulate the geometry of inelastic p+Pb collisions and calculate the probability distribution for the number of participants N_{part}, $P(N_{\mathrm{part}})$. The simulations used a Woods-Saxon nuclear density distribution and an inelastic nucleon-nucleon cross-section of $\sigma_{\mathrm{NN}} = 70 \pm 5$ mb. Separately, PYTHIA8 [22, 23] simulations of pp events (version 8.150, 4C tune [24], MSTW2008LO PDFs [25]) were used to obtain a detector-level $\Sigma E_{\mathrm{T}}^{\mathrm{Pb}}$ distribution for nucleon-nucleon collisions, to be used as input to the Glauber model. This was fit to a gamma distribution.

Then, an extension of the wounded-nucleon (WN) [26] model that included non-linear dependence of $\Sigma E_{\mathrm{T}}^{\mathrm{Pb}}$ on N_{part} was used to define N_{part}-dependent gamma distributions for $\Sigma E_{\mathrm{T}}^{\mathrm{Pb}}$, with the constraint that the distributions reduce to the PYTHIA8 distribution for $N_{\mathrm{part}} = 2$. The non-linear term accounted for the possible variation of the effective FCal acceptance resulting from an N_{part}-dependent backward rapidity shift of the produced soft particles with respect to the nucleon-nucleon frame [27]. The gamma distributions were summed over N_{part} with a $P(N_{\mathrm{part}})$ weighting to produce a hypothetical $\Sigma E_{\mathrm{T}}^{\mathrm{Pb}}$ distribution. That distribution was fit to the measured $\Sigma E_{\mathrm{T}}^{\mathrm{Pb}}$ distribution shown in Fig. 1 with the parameters of the extended WN model allowed to vary freely. From the results of the fit, the distribution of N_{part} values and the corresponding $\langle N_{\mathrm{part}} \rangle$ were calculated for each centrality interval. The resulting R_{coll} and T_{pA} values and corresponding systematic uncertainties are shown in Table 1.

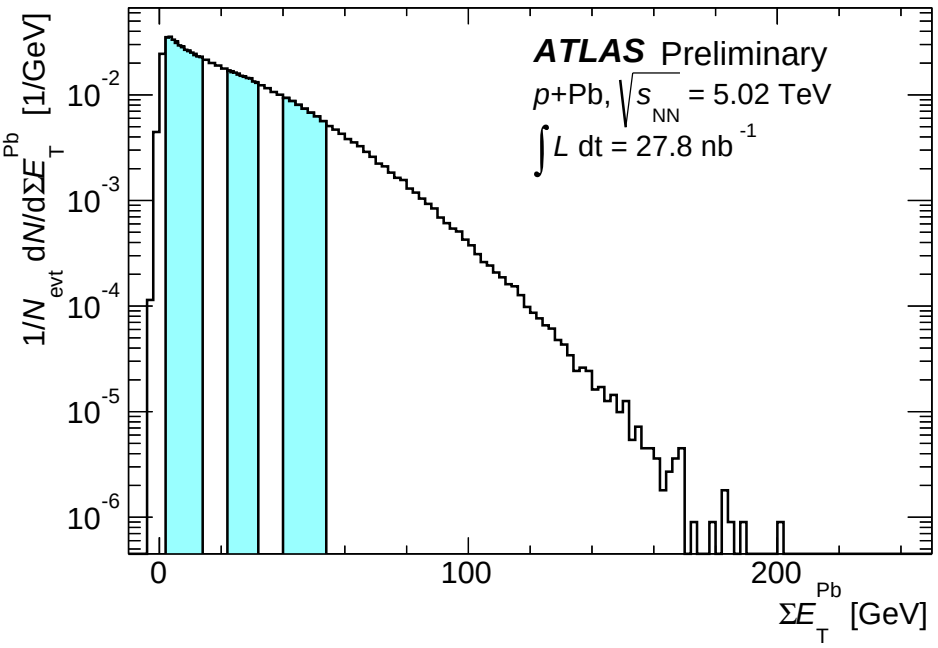

Figure 1: $\Sigma E_{\mathrm{T}}^{\mathrm{Pb}}$ distribution for minimum-bias p+Pb collisions recorded during the 2013 run, measured in the FCal at $3.2 < \eta < 4.9$ in the Pb-going direction. The vertical divisions correspond to the six centrality intervals used in this analysis. From right to left, the regions correspond to: 0–10%, 10–20%, 20–30%, 30–40%, 40–60% and 60–90% p+Pb events.

5 Monte Carlo simulation

The performance of the jet reconstruction procedure was evaluated using a sample of 36 million Monte Carlo events in which simulated $\sqrt{s} = 5.02$ TeV pp hard scattering events were overlaid with minimum-bias p+Pb events recorded during the 2013 run. The MC events were generated using PYTHIA6 [22] (version 6.425, AUET2B tune [24], CTEQ6L1 parton distribution functions [28]) and the detector effects were fully simulated [29] using GEANT4 [30]. Several samples of such events were produced for different intervals of generator-level ("truth") $R = 0.4$ jet p_{T}. In total, the generator-level spectrum spans $10 < p_{\mathrm{T}} < 10^3$ GeV. Separate sets of 18 million events each were generated for the two different beam directions to take into account any z asymmetries in the ATLAS detector. For each beam direction, the momentum four-vectors of the generated particles were longitudinally boosted by a rapidity of ±0.465 to match the corresponding beam conditions. The events were simulated using data conditions appropriate to the two periods of the 2013 p+Pb run and reconstructed using the same algorithms that were applied to the experimental data. A separate 9 million event MC sample of fully simulated 2.76 TeV PYTHIA6 pp hard scattering events with the same tune and PDF set were used to evaluate the jet performance in $\sqrt{s} = 2.76$ TeV pp collisions during 2013 data taking.

6 Jet reconstruction

The jet reconstruction and underlying event (UE) subtraction procedures were adapted from those used by ATLAS in Pb+Pb collisions, which are described in detail in Refs. [31, 32], and are summarised in the following. Calorimeter cells were combined into towers with segmentation $\Delta\eta \times \Delta\phi = 0.1 \times 0.1$, and the anti-$k_t$ algorithm was applied to the towers. A two-iteration procedure was used to obtain an event-

Centrality	R_{coll}	T_{pA} [mb^{-1}]
0-90%	-	$0.106^{+0.007}_{-0.006}$
60-90%	-	$0.043^{+0.003}_{-0.004}$
40-60%	$2.16^{+0.08}_{-0.07}$	$0.092^{+0.004}_{-0.006}$
30-40%	$3.00^{+0.21}_{-0.14}$	$0.126^{+0.003}_{-0.004}$
20-30%	$3.48^{+0.33}_{-0.18}$	$0.148^{+0.004}_{-0.002}$
10-20%	$4.05^{+0.49}_{-0.21}$	$0.172^{+0.007}_{-0.003}$
0-10%	$4.89^{+0.83}_{-0.27}$	$0.208^{+0.019}_{-0.005}$

Table 1: Average R_{coll} and T_{pA} values for the centrality intervals used in this analysis along with total relative systematic uncertainties. The R_{coll} values are with respect to 60-90% events, where $\langle N_{\mathrm{coll}} \rangle = 2.98^{+0.206}_{-0.293}$.

by-event estimate of the UE energy density while excluding contributions from jets to that estimate. This estimate of the UE was constructed separately in each calorimeter layer and in $\Delta\eta = 0.1$ strips to accommodate the η-dependent variations in the UE activity present in p+Pb collisions. For each tower included in a given jet, the estimated UE energy for each cell in the tower was subtracted to correct the cell energy. The jet kinematics were then constructed to be the four-vector sum of all such cells in the jet, taking the cell four-vectors to be massless. The mean subtracted UE transverse energy in p+Pb collisions was 2.4 GeV (1.4 GeV) for $R = 0.4$ jets with $|y^*| < 1$ ($y^* > 3$). In pp collisions, this procedure subtracts the energy deposited in the calorimeter attributed to additional pp interactions in the same crossing (in-time pileup).

After the results of this procedure, a small correction, typically a few percent, was applied to the transverse momentum of those jets which were erroneously included in the initial estimate of the UE background. Finally, the jet energies were corrected to account for the calorimeter energy response using an η- and p_{T}-dependent multiplicative factor that was derived from the simulations [33].

7 Performance

The jet reconstruction performance was evaluated in the MC samples by applying the same subtraction and reconstruction procedure as was applied to data. The resulting set of reconstructed jets was compared with their corresponding generator jets, which were produced by applying the anti-k_t algorithm to the final-state particles produced by PYTHIA, excluding muons and neutrinos. Each generator jet was matched to a reconstructed jet, and the difference in p_{T} between the two jets was studied as a function of generator jet p_{T} and y^*, and in the six p+Pb event centrality intervals. The reconstruction efficiency for jets having $p_{\mathrm{T}} > 25$ GeV is greater than 99%. The performance was quantified by the means and standard deviations of the $\Delta p_{\mathrm{T}}/p_{\mathrm{T}} \left(= p_{\mathrm{T}}^{\mathrm{reco}}/p_{\mathrm{T}}^{\mathrm{gen}} - 1\right)$ distributions, referred to as the jet energy scale (JES) closure and jet energy resolution (JER), respectively. The JES closure in p+Pb events is better than 2% for all $p_{\mathrm{T}} > 25$ GeV jets and is better than 1% for $p_{\mathrm{T}} > 100$ GeV jets. At low p_{T}, the JES closure and JER exhibit a weak p+Pb centrality dependence, with differences in the JES of up to 1% and a larger JER dependence of up to 2% in the most central 0–10% events relative to the 60–90% peripheral events. In pp events, the JES closure is better than 1% in the entire kinematic range studied.

In order to quantify the degree of p_{T} bin migration introduced by the reconstruction procedure and

detector response, response matrices were populated by recording the p_{T} of each generator-reconstructed jet pair. Separate matrices were constructed for each y^* interval and p+Pb centrality used in the analysis. For the p_{T} ranges studied, the proportion of jets with reconstructed p_{T} in the same bin as their truth p_{T} monotonically increases with truth p_{T} and is 50-70%. The increased UE activity in central events relative to peripheral events leads to a slightly larger resolution and energy scale non-closure in these events for low p_{T} jets, resulting in larger bin migration effects. At high jet p_{T}, where the role of the underlying event becomes less important than the intrinsic calorimetric resolution on the jet energy, the response is centrality independent within systematic uncertainties.

8 Data analysis

Jets in p+Pb collisions were selected by the minimum-bias triggers and jet triggers described above. In total, six jet triggers with different online jet p_{T} thresholds were used in p+Pb data-taking for jets with $|\eta| < 3.2$ and one dedicated low-threshold trigger was used for jets with $|\eta| > 3.2$. The sampled luminosity (defined as the luminosity divided by the mean luminosity-weighted prescale) of the triggers increases with increasing p_{T} threshold. Offline jets were selected for the analysis by requiring a match to an online jet trigger. The efficiency of the various triggers was determined with respect to the minimum-bias trigger and to low-p_{T} jet triggers. For simplicity, each p_{T} bin was filled with jets selected by only one trigger. In a given p_{T} bin, jets were selected by the lowest-threshold jet trigger for which the efficiency has been determined to be greater than 99% in the bin. No additional corrections for the trigger efficiency were applied.

The double differential per-event jet yields in p+Pb collisions are constructed via

$$\frac{1}{N_{\mathrm{evt}}}\frac{\mathrm{d}^2N^{\mathrm{jet}}}{\mathrm{d}p_{\mathrm{T}}dy^*} = \frac{1}{N_{\mathrm{evt}}}\frac{N^{\mathrm{jet}}}{\Delta p_{\mathrm{T}}\Delta y^*} \tag{3}$$

where N_{evt} is the total (unprescaled) number of MB p+Pb events sampled by ATLAS, N^{jet} is the yield of jets corrected for all detector effects and the instantaneous trigger prescale during data-taking, and Δp_{T} and Δy^* are the widths of the p_{T} and y^* bins. The centrality-dependent yields are constructed by restricting N_{evt} and N^{jet} to come from p+Pb events with a given range of $\Sigma E_{\mathrm{T}}^{\mathrm{Pb}}$. The double differential cross-section in pp collisions is constructed via

$$\frac{\mathrm{d}^2\sigma}{\mathrm{d}p_{\mathrm{T}}dy^*} = \frac{1}{L_{\mathrm{int}}}\frac{N^{\mathrm{jet}}}{\Delta p_{\mathrm{T}}\Delta y^*} \tag{4}$$

where L_{int} is the total integrated luminosity of the jet trigger used in the given p_{T} bin. The p_{T} binning in the pp cross-section was chosen such that the $x_{\mathrm{T}} = 2p_{\mathrm{T}}/\sqrt{s}$ binning between p+Pb and pp is the same.

Both the per-event yields in p+Pb collisions and the cross-section in pp collisions are restricted to the p_{T} range where the MC studies described above have determined that the efficiency for a truth jet to remain in the same p_{T} bin is $\geq 50\%$. This p_{T} range is rapidity dependent, reaching a smaller p_{T} at more forward rapidities.

The measured p+Pb and pp yields are corrected for jet energy resolution and residual distortions of the jet energy scale in each rapidity interval by the use of p_{T}- and y^*-dependent (and, in the p+Pb case, centrality dependent) bin-by-bin correction factors $C(p_{\mathrm{T}}, y^*)$ obtained from the ratio of the reconstructed and truth jet distributions, according to

$$C(p_{\mathrm{T}}, y^*) = \frac{N^{\mathrm{jet}}_{\mathrm{truth}}(p_{\mathrm{T}}, y^*)}{N^{\mathrm{jet}}_{\mathrm{reco}}(p_{\mathrm{T}}, y^*)} \tag{5}$$

where $N^{\text{jet}}_{\text{truth}}$ ($N^{\text{jet}}_{\text{reco}}$) is the number of truth jets in the given $p^{\text{truth}}_{\text{T}}$ ($p^{\text{reco}}_{\text{T}}$) bin in the corresponding MC samples.

Since the determination of the correction factors $C(p_{\text{T}}, y^*)$ is sensitive to the shape of the MC truth jet distribution, the response matrices used to generate them were reweighted to provide a better match between the reconstructed MC and data distributions. The spectrum of generator jets is weighted by the ratio of the reconstructed spectrum in data to that in simulation. This ratio was found to be approximately linear in the logarithm of p_{T}. A separate reweighting was performed for the p+Pb jet yield in each centrality interval, resulting in changes of $\leq 10\%$ from the original correction factors before reweighting. The resulting corrections to the p+Pb and pp yields are at most 30%, and are typically $\leq 10\%$ for jets with $p_{\text{T}} > 100$ GeV. These corrections are applied to the detector-level yield $N^{\text{jet}}_{\text{reco}}$ to give the particle-level yield via

$$N^{\text{jet}} = C(p_{\text{T}}, y^*) N^{\text{jet}}_{\text{reco}}. \tag{6}$$

A $\sqrt{s} = 5.02$ TeV pp reference jet cross-section is constructed through the use of the corrected 2.76 TeV pp cross-section and an ATLAS measurement of the x_{T}-scaling between the $\sqrt{s} = 2.76$ TeV and 7 TeV pp jet cross-sections [34]. In this measurement, the $\sqrt{s}$-scaled ratio ρ of the 2.76 TeV and 7 TeV cross-sections was evaluated at fixed x_{T},

$$\rho(x_{\text{T}}; y^*) = \left(\frac{2.76\text{ TeV}}{7\text{ TeV}}\right)^3 \frac{\mathrm{d}^2\sigma^{2.76\text{ TeV}}/\mathrm{d}p_{\text{T}}dy^*}{\mathrm{d}^2\sigma^{7\text{ TeV}}/\mathrm{d}p_{\text{T}}dy^*}, \tag{7}$$

where $\mathrm{d}^2\sigma^{\sqrt{s}}/\mathrm{d}p_{\text{T}}dy^*$ is the pp jet cross-section at the given centre-of-mass energy $\sqrt{s}$, and the numerator and denominator are each evaluated at the same x_{T} (but different $p_{\text{T}} = x_{\text{T}}\sqrt{s}/2$) bin. Equation 7 can be rearranged to define the cross-section at $\sqrt{s} = 7$ TeV in terms of that at 2.76 TeV times a multiplicative factor and ρ^{-1}.

The $\sqrt{s} = 5.02$ TeV pp cross-section at each p_{T} and y^* bin is constructed by scaling the corrected $\sqrt{s} = 2.76$ TeV pp cross-section measured at the equivalent x_{T} according to

$$\frac{\mathrm{d}^2\sigma^{5.02\text{ TeV}}}{\mathrm{d}p_{\text{T}}dy^*} = \rho(x_{\text{T}}; y^*)^{-0.643} \left(\frac{2.76\text{ TeV}}{5.02\text{ TeV}}\right)^3 \frac{\mathrm{d}^2\sigma^{2.76\text{ TeV}}}{\mathrm{d}p_{\text{T}}dy^*} \tag{8}$$

where the power is $-\ln(2.76/5.02)/\ln(2.76/7) \approx -0.643$ instead of -1 since it interpolates the x_{T}-dependent change in the index of the power-law spectrum from $\sqrt{s} = 2.76$ TeV and 7 TeV to 5.02 TeV. Since the energy scale and x_{T} interpolation uncertainties are large for the pp data at large rapidities ($|y^*| > 2.8$), a $\sqrt{s} = 5.02$ TeV reference is not constructed in that rapidity region. The pp jet cross-section at $\sqrt{s} = 2.76$ TeV was found to agree within the uncertainties of the previous measurement of the same quantity by ATLAS using 0.20 pb^{-1} of data collected in 2011 [34]. In most of the rapidity bins within $|y^*| < 2.8$, the central values of the two measurements agree to within 5%.

9 Systematic uncertainties

The R_{CP} and R_{pPb} measurements are subject to systematic uncertainties arising from a number of sources: the jet energy scale (JES) and resolution (JER), the bin-by-bin corrections from the differences in the spectral shape between data and simulation, residual inefficiency in the trigger selection, and the estimates of the geometric quantities R_{coll} (in the R_{CP}) and T_{pA} (in the R_{pPb}). In addition to these sources of uncertainty which are common to the R_{CP} and R_{pPb} measurements, the R_{pPb} is also subject to uncertainties from the x_{T}-interpolation of the $\sqrt{s} = 2.76$ TeV pp cross-section to the $\sqrt{s} = 5.02$ TeV centre-of-mass energy, and from the integrated luminosity of the pp data set.

Uncertainties in the JES and JER influence the correction of the p+Pb and pp jet spectra. The uncertainty in the JES is taken from *in situ* ATLAS studies of the calorimeter response and systematic variations of the jet response in MC simulation [33], as well as studies of the relative energy scale difference between the jet reconstruction procedure in heavy ion collisions and the procedure used in ATLAS inclusive jet measurements in 2.76 TeV and 7 TeV pp collisions [34, 35]. The JES uncertainty is $\lesssim 4\%$ for jets in the measured p_{T} range in $|y^*| < 2.8$, and $\lesssim 7\%$ for jets in $|y^*| > 2.8$. The effect of this uncertainty on the measurement is evaluated by varying the reconstructed jet p_{T} in MC simulations up and down by the JES uncertainty. The uncertainty in the JER is taken from *in situ* studies of the dijet energy balance [36]. The JER uncertainty is generally $< 10\%$, except for low-p_{T} jets where it is $< 20\%$. The effects on the R_{CP} and R_{pPb} are evaluated through an additional smearing of the energy of reconstructed jets in the simulation such that this uncertainty is added to the original resolution in quadrature.

The resulting systematic uncertainties in the R_{CP} (δR_{CP}) and R_{pPb} (δR_{pPb}) were evaluated by producing new response matrices in accordance with the JES and JER uncertainties, generating new correction factors, and calculating the new R_{CP} and R_{pPb} results. Each JES and JER variation was applied to all rapidity bins and to both p+Pb and pp response matrices simultaneously. Since the correction factors for the p+Pb spectra in different centrality intervals are affected to a similar degree by variations in the JES and JER, the effects tend to cancel in the R_{CP} ratio, and the resulting δR_{CP} are small. The resulting δR_{pPb} values are somewhat larger than the δR_{CP} values due to the relative centre of mass shift between the p+Pb and pp collision systems. The centrality dependence of the JES and JER uncertainties in p+Pb events is negligible.

Differences in the spectral shape between data and MC create the need to reweight the MC for better correspondence with the data before deriving the bin-by-bin correction factors. To be conservative, the entire change in the results introduced by the reweighting is taken as a systematic uncertainty. Thus, the R_{CP} and R_{pPb} are determined using the correction factors before and after reweighting, with the differences δR_{CP} and δR_{pPb} added to the total systematic uncertainty.

As the jet triggers used for the data selection have been evaluated to have greater than 99% efficiency in the p_{T} regions where they are used to select jets, an uncertainty of 1% is chosen for the centrality selected p+Pb yields and the pp cross-section in the range $20 < p_{\mathrm{T}} < 125$ GeV. This uncertainty is conservatively taken to be uncorrelated between the centrality-selected p+Pb yields and the pp cross-section, resulting in a 1.4% uncertainty on the R_{CP} and R_{pPb} when added in quadrature from the numerator and denominator in these ratios.

The geometric quantities R_{coll} and T_{pA} and their uncertainties are listed in Table 1. These arise from uncertainties in the geometric modeling of p+Pb collisions and modeling the N_{part}-dependence of the forward particle production measured in the $\Sigma E_{\mathrm{T}}^{\mathrm{Pb}}$. In general, the uncertainties are asymmetric. Uncertainties in R_{coll} are largest for the most central to the most peripheral ratio (0-10%/60-90%), where they are +17/-6%, and smallest in the 40-60%/60-90% ratio, where they are +4/-3%. Uncertainties in T_{pA} are largest in the most central (0-10%) and most peripheral (60-90%) centrality intervals, where the upper or lower uncertainty can reach 10%, and smaller for intervals in the middle of the p+Pb centrality range, where they reach a minimum of +3/-2% for the 20-30% interval.

The x_{T}-interpolation of the $\sqrt{s} = 2.76$ TeV pp jet cross-section to 5.02 TeV is sensitive to uncertainties in $\rho(x_{\mathrm{T}}, y^*)$, the $\sqrt{s}$-scaled ratio of jet spectra at 2.76 and 7 TeV. Following Eq. 8, the uncertainty in the interpolated pp cross-section ($\delta\sigma^{5.02\ \mathrm{TeV}}$) at fixed x_{T} is related to the uncertainty in ρ ($\delta\rho$) via $(\delta\sigma^{5.02\ \mathrm{TeV}}/\sigma^{5.02\ \mathrm{TeV}}) = 0.643(\delta\rho/\rho)$, where $\delta\rho$ is taken from Ref. [34]. $\delta\rho$ ranges from 5% to 23% in the region of the measurement and is generally larger at lower x_{T} and at larger rapidities.

The integrated luminosity for the 2013 pp data-taking was calculated by measuring the interaction rate with several ATLAS subdetectors. The absolute calibration was derived from three van der Meer scans [37] performed during the pp data-taking in 2013 in an analysis similar to what has been previ-

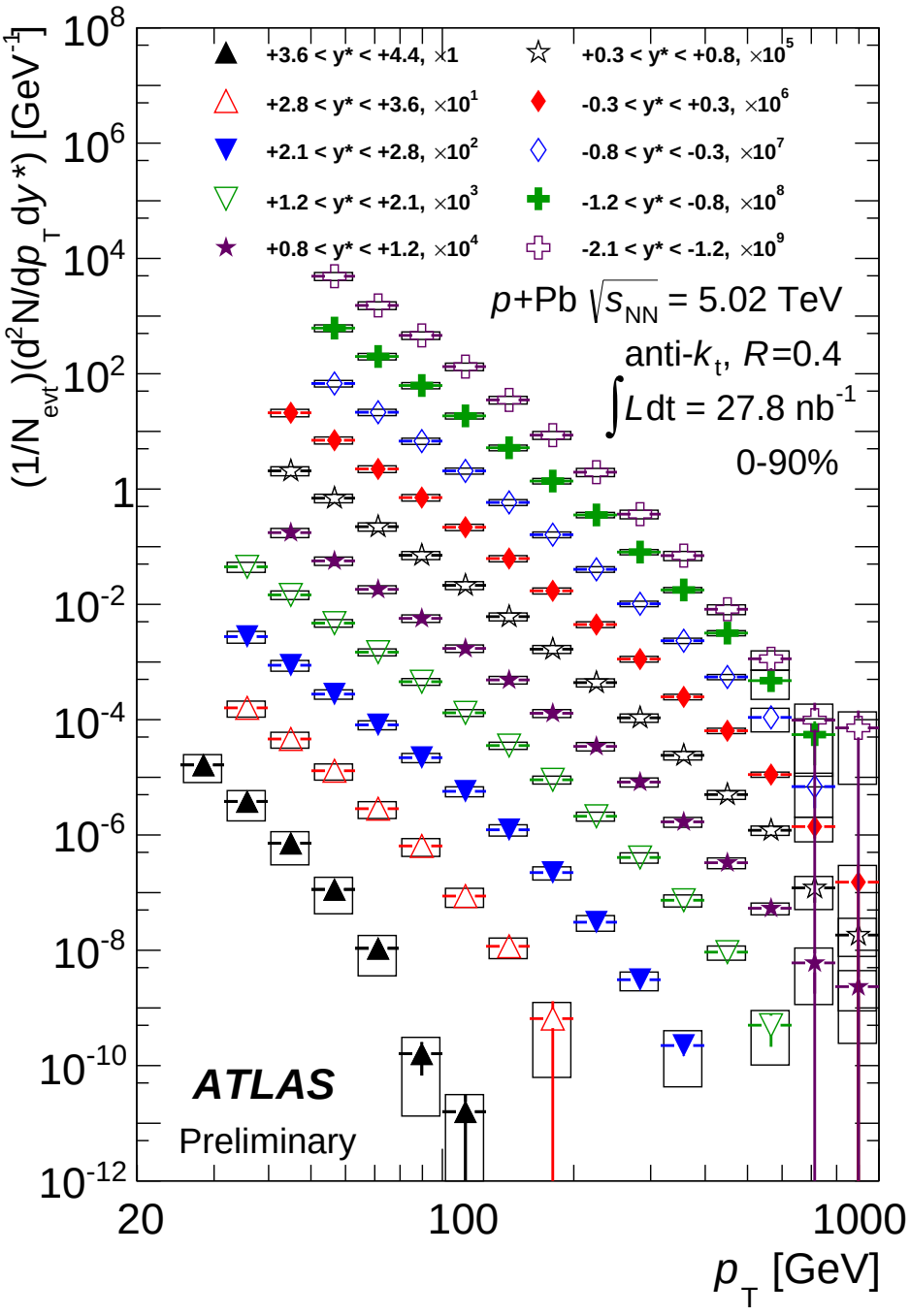

Figure 2: Inclusive double differential per-event jet yield in 0–90% p+Pb collisions as a function of jet p_{T} in different y^* bins. The yields are corrected for all detector effects. Vertical error bars represent the statistical uncertainty while the boxes represent the systematic uncertainties.

ously done for pp data-taking at higher energies within ATLAS [38]. The systematic uncertainty on the integrated luminosity is estimated to be 3.4%.

The uncertainties from the JES, JER, shape and x_{T}-interpolation are p_{T} and y^* dependent, while the uncertainties from the trigger, luminosity, and geometric factors are not. The total systematic uncertainty on the R_{pPb} ranges from 6% at mid-rapidity and high p_{T}, to 18% at forward rapidities and low p_{T}. In most p_{T} and rapidity bins, the dominant systematic uncertainty on the R_{pPb} is from the x_{T}-interpolation. The p_{T} and y^* dependent systematic uncertainties on the R_{CP} are small. Near mid-rapidity or at high p_{T}, they are 2%, rising to approximately 10% at low p_{T} in forward rapidities. Thus, in most of the kinematic region studied, the dominant uncertainty on the R_{CP} is from the geometric factors R_{coll}.

10 Results

Figure 2 presents the fully corrected per-event jet yield as a function of p_{T} in 0–90% p+Pb collisions, for each of the jet centre-of-mass rapidity ranges used in this analysis. At mid-rapidity, the yields span over eight orders of magnitude.

The R_{pPb} for jets in 0–90% p+Pb events is presented in Fig. 3 in the eight rapidity bins for which a pp reference was constructed. At most rapidities studied, the R_{pPb} shows a slight ($\approx 10\%$) enhancement above 1, although many bins are consistent with unity within the systematic uncertainties. At mid-rapidity, the R_{pPb} is at a maximum near 100 GeV. No large modification of the total yield of jets relative to the geometric expectation is observed. The data in Fig. 3 are compared to an NLO pQCD calculation of the R_{pPb}using the EPS09 parameterisation of nuclear parton distribution functions [9]. The data are slightly higher but generally compatible with the calculation within systematics.

Figure 4 shows examples of the centrality-selected p+Pb yields in three centrality intervals and three rapidity ranges.

The central-to-peripheral ratio R_{CP} for jets in p+Pb collisions is summarised in Fig. 5, where three centrality intervals are shown in ratio to peripheral (60–90%) events at all rapidity ranges studied. The R_{CP} shows a strong variation with centrality relative to the geometric expectation. The 0-10%/60-90% R_{CP} for jets is smaller than 1 at all rapidities for jet $p_{\mathrm{T}} > 100$ GeV and at all p_{T} at sufficiently forward rapidity. Near mid-rapidity, the 40-60%/60-90% R_{CP} is consistent with unity up to 100-200 GeV, but indicates a small suppression at higher p_{T}. In all rapidity bins studied, the R_{CP} decreases with increasing p_{T} and in increasingly more central collisions. Furthermore, at fixed p_{T}, the R_{CP} decreases systematically at more forward (proton-going) rapidities. At the highest p_{T} in the most forward rapidity bin, the 0–10%/60–90% R_{CP} reaches a value of ≈ 0.2. In the backward rapidity direction ($y^* < 0$), the R_{CP} is found to be enhanced by 10–20% for low p_{T} jets.

Figure 6 summarises the R_{pPb} in central, mid-central and peripheral events in all rapidity bins studied. The patterns observed in the centrality-dependent R_{pPb} are a consequence of the near geometric scaling observed in the 0–90% R_{pPb} along with the strong modifications observed in the central-to-peripheral ratio R_{CP}. At sufficiently high-p_{T}, the R_{pPb} in central events is found to be suppressed ($R_{\mathrm{pPb}} < 1$) and in peripheral events to be enhanced ($R_{\mathrm{pPb}} > 1$). Furthermore, these respective deviations from the geometric expectation (under which $R_{\mathrm{pPb}} = 1$) generally increase with p_{T} and, at fixed p_{T}, generally increase with more forward rapidity ranges. Thus, the large effects in the R_{CP} are consistent with a combination of modifications that have opposite sign in the centrality-dependent R_{pPb} but little effect in the centrality-inclusive 0–90% R_{pPb}. At backward going rapidities ($y^* < 0$) the R_{pPb} for low p_{T} jets in all centralities is consistent within the uncertainties with unity.

Given the observed suppression pattern as a function of jet rapidity, in which the suppression in the R_{CP} at fixed p_{T} systematically increases at more forward going rapidities, it is natural to ask if it is possible to find a single relationship between the R_{CP} in the different rapidity bins that is a function of jet kinematics alone. To test this, the R_{CP} in each rapidity bin is plotted against the quantity $p_{\mathrm{T}} \times \cosh(\langle y^* \rangle) \approx$

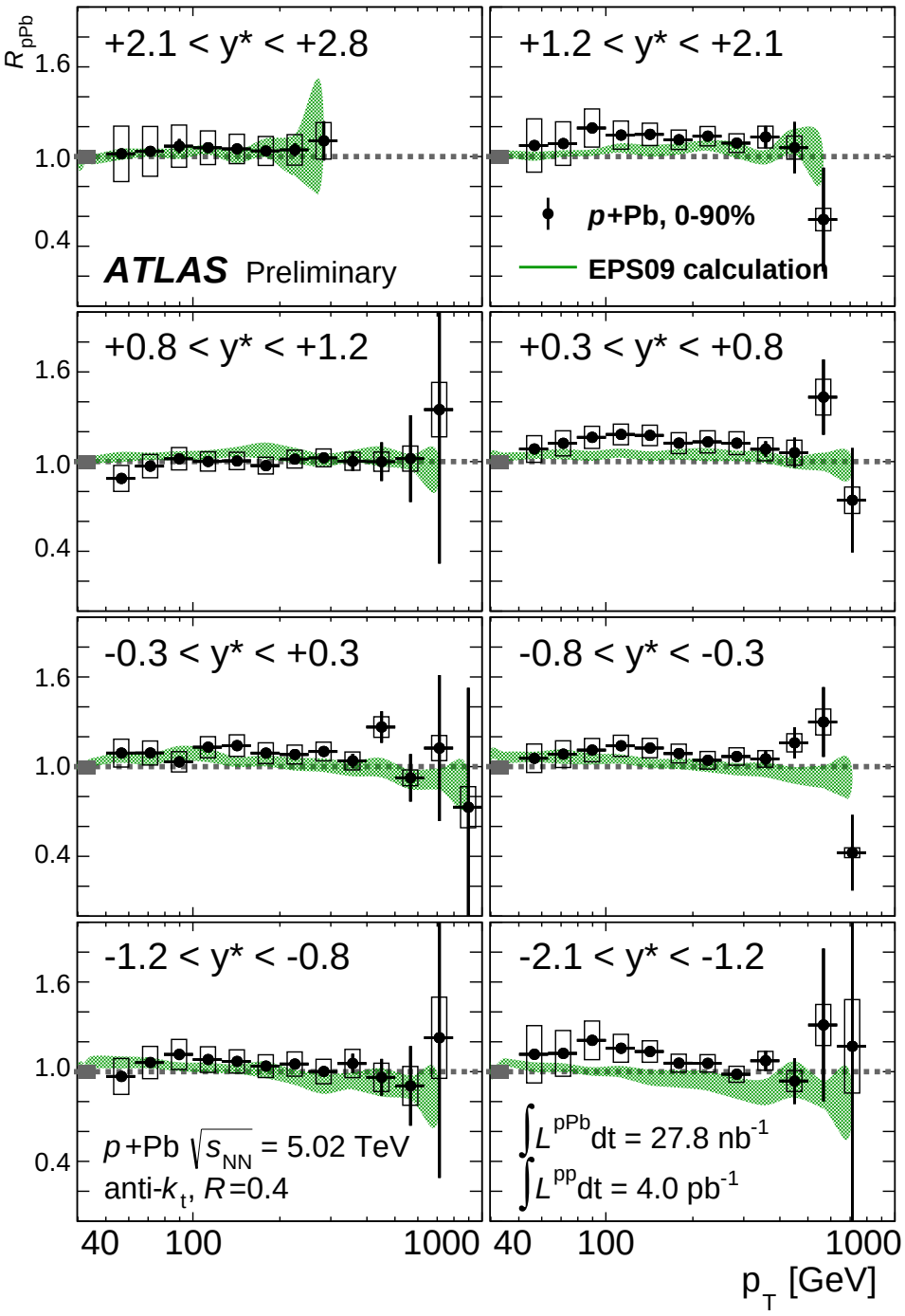

Figure 3: R_{pPb} for $R = 0.4$ jets in 0–90% $\sqrt{s_{\mathrm{NN}}} = 5.02$ TeV p+Pb collisions. Each panel shows the jet R_{pPb} at a different rapidity range. Vertical error bars and boxes around the data points represent statistical and systematic uncertainties, respectively. The green band represents a calculation using the EPS09 nuclear parton distribution function set. The shaded gray box on left edge of the $R_{\mathrm{pPb}} = 1$ horizontal line indicates the systematic uncertainty on T_{pA} and the pp luminosity in quadrature.

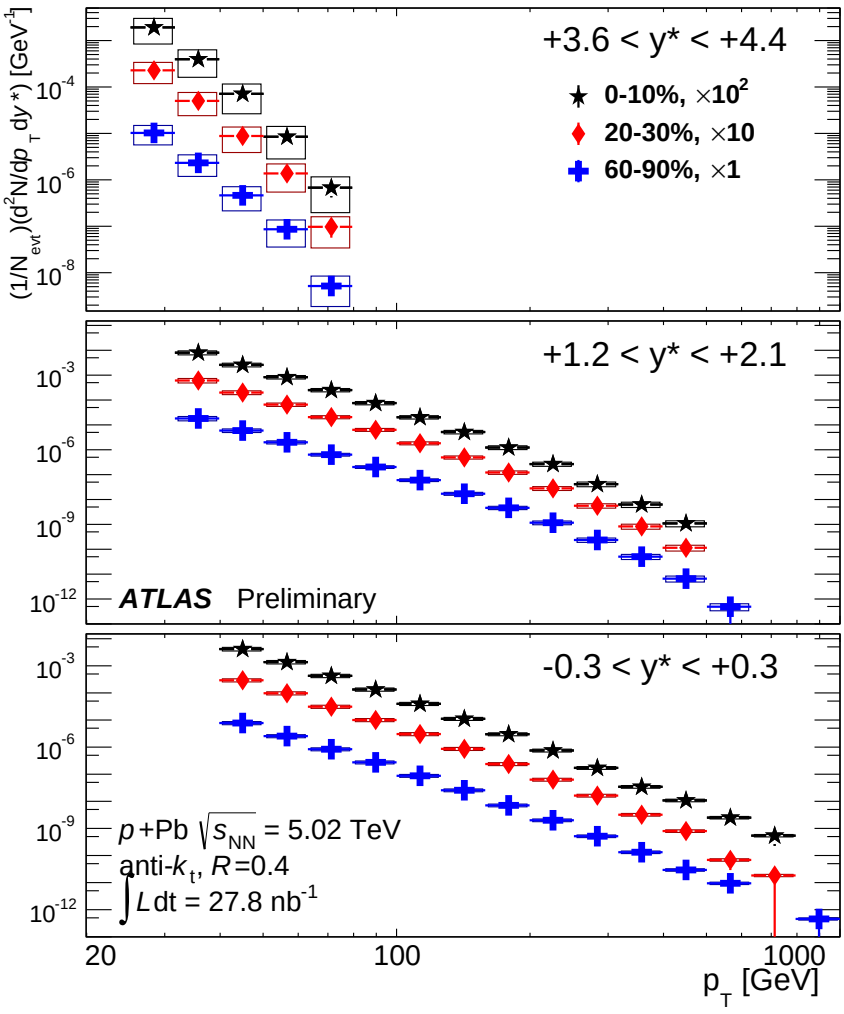

Figure 4: Centrality-dependent inclusive double differential per-event jet yield in p+Pb collisions, at three different rapidity ranges. Each panel shows the yield in central (black), mid-central (red) and peripheral (blue) events. The yields are corrected for all detector effects. Vertical error bars represent the statistical uncertainty while the boxes represent the systematic uncertainties.

p, where y^* is the centre of the rapidity bin, and p is therefore approximately the total energy of the jet. The 0–10%/60–90% $R_{\rm CP}$ versus $p_{\rm T} \times \cosh(\langle y^* \rangle)$ is plotted for all ten rapidity ranges in Fig. 7. When plotted against this variable, the $R_{\rm CP}$ in each of the five forward-going rapidities ($y^* > +0.8$) falls along the same curve, which is approximately linear in the logarithm of p. This trend is also observed in the two most forward of the remaining rapidity bins ($-0.3 < y^* < +0.8$), but the $R_{\rm CP}$ at backward rapidities ($y^* < -0.3$) does not observe this trend. This pattern was also observed in other centrality intervals, albeit with a different slope in $\ln(p)$ for each centrality interval.

These patterns suggests that the observed modifications may be a function of the initial parton kinematics, such as the longitudinal momentum fraction of the parton in the proton x_p. In particular, a dependence on x_p would explain why the data follow a consistent trend vs. $p_{\rm T} \cosh(\langle y^* \rangle)$ at forward rapidities (where jet production at a given jet energy p is dominated by $x_p \sim p/(\sqrt{s}/2)$ partons in the proton) but do not do so at backward rapidities (where x_{Pb} as well as x_p are needed to relate the jet and parton kinematics).

By analogy with the plot of the $R_{\rm CP}$ plotted against $p_{\rm T} \cosh(\langle y^* \rangle)$, the $R_{\rm pPb}$ in the four most forward-

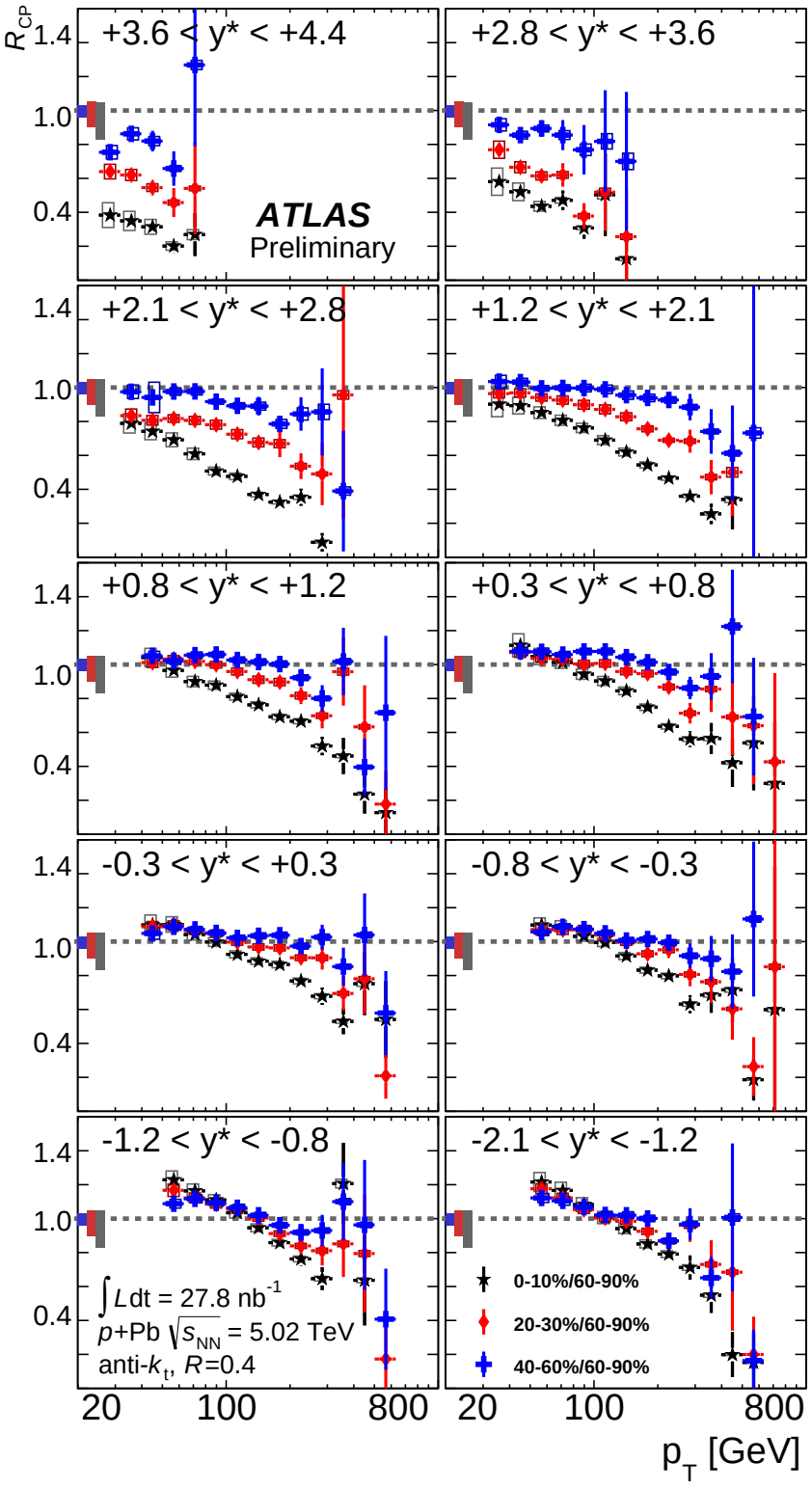

Figure 5: R_{CP} for $R = 0.4$ jets in $\sqrt{s_{\mathrm{NN}}} = 5.02$ TeV p+Pb collisions in central (black), mid-central (red) and mid-peripheral (blue) events. Each panel shows the jet R_{CP} at a different rapidity range. Vertical error bars represent the statistical uncertainty while the boxes represent the systematic uncertainties. The shaded boxes on the left edge of the $R_{\mathrm{CP}} = 1$ horizontal line indicate the systematic uncertainty on R_{coll} for the corresponding centrality intervals of the same color.

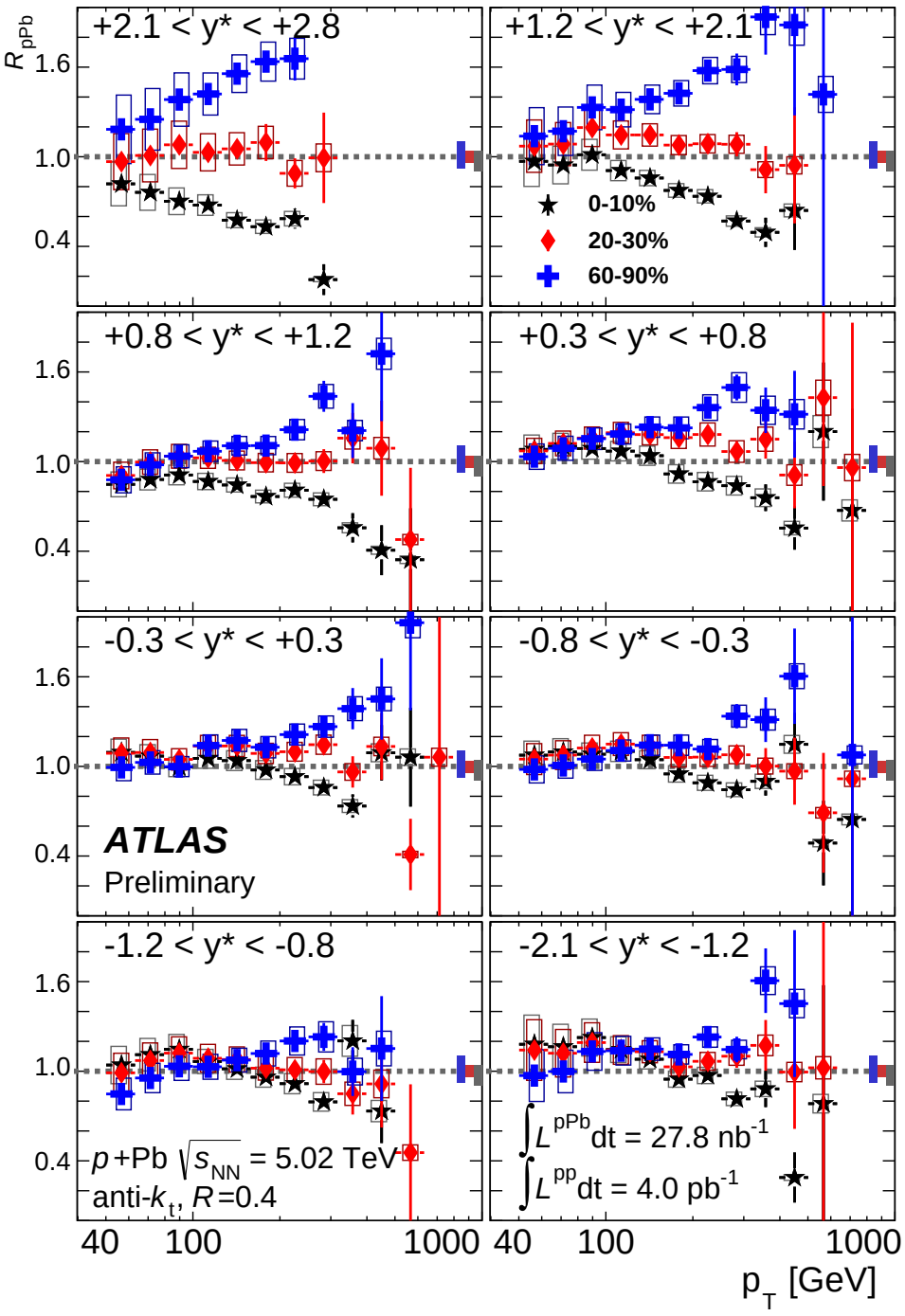

Figure 6: R_{pPb} for $R = 0.4$ jets in $\sqrt{s_{\mathrm{NN}}} = 5.02$ TeV p+Pb collisions in central (black), mid-central (red) and peripheral (black) events. Each panel shows the jet R_{pPb} at a different rapidity range. Vertical error bars represent the statistical uncertainty while the boxes represent the systematic uncertainties. The shaded boxes on the right edge of the $R_{\mathrm{pPb}} = 1$ horizontal line indicate the systematic uncertainty on T_{pA} and the pp luminosity in quadrature.

going bins studied is shown plotted against this variable in Fig. 8. The R_{pPb} in central and peripheral events are shown separately. Although the systematic uncertainties are larger on the R_{pPb} than the R_{CP},

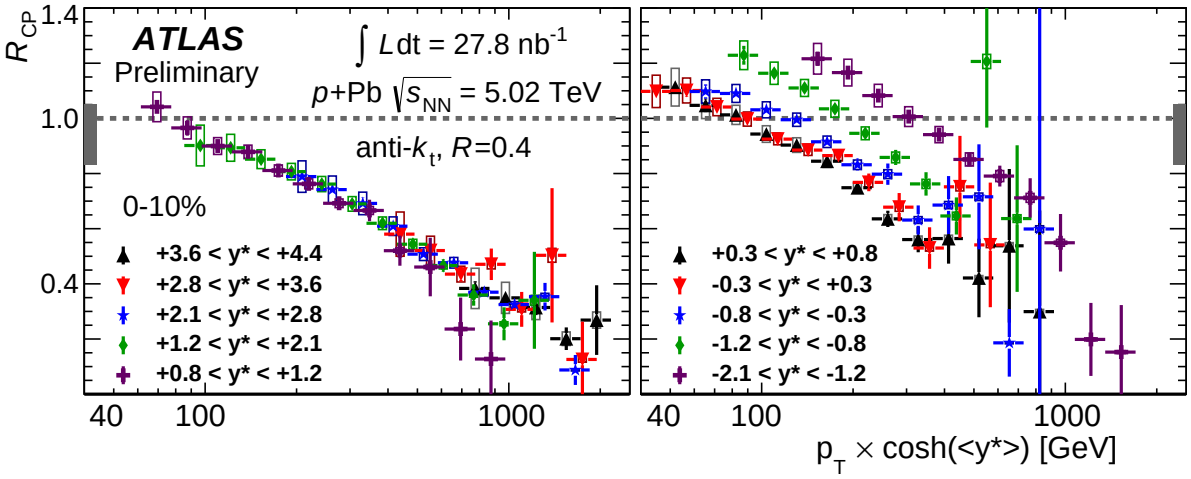

Figure 7: R_{CP} for $R = 0.4$ jets in 0–10% $\sqrt{s_{\mathrm{NN}}} = 5.02$ TeV p+Pb collisions. The panel on the left shows the five rapidity ranges that are most forward going, while the panel on the right shows the remaining five. The R_{CP} at each rapidity is plotted as a function of $p_{\mathrm{T}} \times \cosh(\langle y^* \rangle)$, where $\langle y^* \rangle$ is the midpoint of the rapidity bin. Vertical error bars represent the statistical uncertainty while the boxes represent the systematic uncertainties. The shaded box on the left edge (in the left panel) and right edge (in the right panel) of the $R_{\mathrm{CP}} = 1$ horizontal line indicates the systematic uncertainty on R_{coll}.

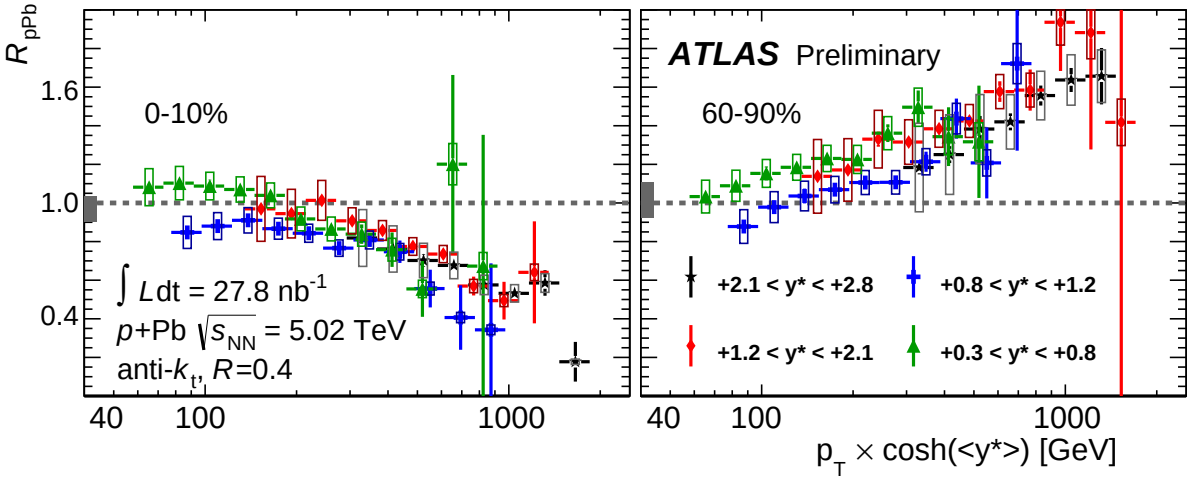

Figure 8: R_{pPb} for $R = 0.4$ jets in $\sqrt{s_{\mathrm{NN}}} = 5.02$ TeV p+Pb collisions at multiple rapidity ranges, showing 0–10% events in the left panel and 60–90% events in the right panel. The R_{pPb} at each rapidity is plotted as a function of $p_{\mathrm{T}} \times \cosh(\langle y^* \rangle)$, where $\langle y^* \rangle$ is the midpoint of the rapidity bin. Vertical error bars represent the statistical uncertainty while the boxes represent the systematic uncertainties. The shaded box on the left edge of the $R_{\mathrm{pPb}} = 1$ horizontal line indicates the systematic uncertainty on T_{pA} and the pp luminosity in quadrature.

the observed behavior for jets with $p_{\mathrm{T}} > 150$ GeV is consistent with the nuclear modifications depending only on the total jet energy $p_{\mathrm{T}} \cosh(\langle y^* \rangle)$. In central (peripheral) events, the R_{pPb} at forward rapidities is consistent with a rapidity-independent decreasing (increasing) function of $p_{\mathrm{T}} \cosh(\langle y^* \rangle)$. Thus, the single trend in the R_{CP} versus $p_{\mathrm{T}} \cosh(\langle y^* \rangle)$ at forward rapidities is consistent with arising from opposite trends in the central and peripheral R_{pPb} versus $p_{\mathrm{T}} \cosh(\langle y^* \rangle)$.

The results have been presented here using the default Glauber model to estimate the geometric quantities. ATLAS has also studied the impact of geometric models which incorporate event by event changes in the configuration of the proton wavefunction [39]. Using either of these so called "Glauber-Gribov" models to determine the geometric parameters amplifies the effects seen with the Glauber geometric model. The suppression in central events and the enhancement in peripheral events would be increased.

11 Conclusions

This note has presented the results of a measurement of the centrality dependence of jet production in p+Pb collisions at $\sqrt{s_{\mathrm{NN}}} = 5.02$ TeV over a wide kinematic range with the ATLAS detector at the LHC. The centrality of p+Pb collisions was characterised using the total transverse energy measured in the Pb-going forward calorimeter covering the interval $3.2 < \eta < 4.9$. The average number of nucleon-nucleon collisions, $\langle N_{\mathrm{coll}} \rangle$, and the mean nuclear thickness factor, T_{pA}, were evaluated for each centrality interval using a Glauber Monte Carlo analysis.

Results were presented for the nuclear modification factor R_{pPb} with respect to a measurement of the inclusive jet cross-section in $\sqrt{s} = 2.76$ TeV pp collisions x_{T}-interpolated to 5.02 TeV using previous ATLAS measurements of jet production at 2.76 and 7 TeV. Results were also shown for the central-to-peripheral ratio R_{CP}, made with respect to the 60–90% centrality bin. The centrality-inclusive R_{pPb} results for 0–90% collisions indicated only a modest enhancement over the geometric expectation. This enhancement was observed to have a weak p_{T} and rapidity dependence, and to be generally consistent with predictions from the modification of the parton distribution functions in the nucleus.

The results of the R_{CP} measurement indicate a strong, centrality-dependent reduction in the yield of jets in central collisions relative to that in peripheral collisions, after accounting for the effects of collision geometry. In addition, the reduction becomes more pronounced with jet p_{T} and at more forward (downstream proton) rapidities. These two results are reconciled by the centrality-dependent R_{pPb} results, which show a suppression in central collisions and enhancement in peripheral collisions which is systematic in p_{T} and y^*.

The R_{CP} and R_{pPb} data at forward rapidities were replotted as a function of $p_{\mathrm{T}} \cosh(\langle y^* \rangle)$, the approximate total jet energy. When plotted this way, the results from different rapidity bins fall into roughly a single trend. This suggests that the mechanism responsible for the observed effects may depend only on the total jet energy or, more generally, on the underlying parton-parton kinematics such as the fractional longitudinal momentum of the parton originating in the proton x_p.

If the relationship between the centrality intervals and proton-lead collision impact parameter determined within the geometric models is correct, these results imply large, impact parameter-dependent changes in the number of partons available for hard scattering. However, they may also be the result of a correlation between the kinematics of the scattering and the soft interactions resulting in particle production at backward (Pb-going) rapidities[40, 41]. The presence of such correlations would challenge the usual factorisation-based picture for describing hard scattering processes in collisions involving nuclei.

References

[1] C. Salgado et al., J. Phys. **G39** (2012) 015010.

[2] BRAHMS Collaboration, I. Arsene et al., Phys. Rev. Lett. **93** (2004) 242303, arXiv:0403005 [nucl-ex].

[3] PHENIX Collaboration, A. Adare et al., Phys. Rev. Lett. **94** (2005) 082302, arXiv:0411054 [nucl-ex].

[4] STAR Collaboration, J, Adams et al., Phys. Rev. Lett. **97** (2006) 152302, arXiv:0602011 [nucl-ex].

[5] PHENIX Collaboration, A. Adare et al., Phys. Rev. Lett. **107** (2011) 172301.

[6] J. Jalilian-Marian and Y. V. Kovchegov, Prog. Part. Nucl. Phys. **56** (2006) 104–231, arXiv:0505052 [hep-ph].

[7] F. Gelis, E. Iancu, J. Jalilian-Marian, and R. Venugopalan, Ann. Rev. Nucl. Part. Sci. **60** (2010) 463–489, arXiv:1002.0333 [hep-ph].

[8] D. Kharzeev, Y. V. Kovchegov, and K. Tuchin, Phys. Lett. **B599** (2004) 23–31, arXiv:0405045 [hep-ph].

[9] K. Eskola, H. Paukkunen, and C. Salgado, JHEP **0904** (2009) 065, arXiv:0902.4154 [hep-ph].

[10] B. Kopeliovich et al., Phys. Rev. **C72** (2005) 054606, arXiv:0501260 [hep-ph].

[11] J.-W. Qiu and I. Vitev, Phys. Lett. **B632** (2006) 507–511, arXiv:0405068 [hep-ph].

[12] M. Cacciari, G. P. Salam, and G. Soyez, JHEP **0804** (2008) 063, arXiv:0802.1189 [hep-ph].

[13] PHENIX Collaboration, S.S. Adler et al., Phys. Rev. Lett. **98** (2007) 172302, arXiv:0610036 [nucl-ex].

[14] PHOBOS Collaboration, B.B. Back et al., Phys. Rev. **C70** (2004) 061901, arXiv:0406017 [nucl-ex].

[15] M. L. Miller, K. Reygers, S. J. Sanders, and P. Steinberg, Ann. Rev. Nucl. Part. Sci. **57** (2007) 205–243, arXiv:0701025 [nucl-ex].

[16] ATLAS Collaboration, JINST **3** (2008) S08003.

[17] ATLAS Collaboration, Eur. Phys. J. **C70** (2010) 787–821.

[18] ATLAS Collaboration, Eur. Phys. J. **C72** (2012) 1849.

[19] ATLAS Collaboration, New J. Phys. **13** (2010) 053033.

[20] ATLAS Collaboration, Phys. Lett. **B710** (2012) 363–382, arXiv:1108.6027 [hep-ex].

[21] B. Alver, M. Baker, C. Loizides, and P. Steinberg, arXiv:0805.4411 [nucl-ex].

[22] T. Sjostrand, S. Mrenna, and P. Z. Skands, JHEP **05** (2006) 026, arXiv:0603175 [hep-ph].

[23] T. Sjostrand, S. Mrenna, and P. Z. Skands, Comput. Phys. Commun. **178** (2008) 852–867, arXiv:0710.3820 [hep-ph].

[24] ATLAS Collaboration, ATL-PHYS-PUB-2012-003 (2011).

[25] A. Martin, W. Stirling, R. Thorne, and G. Watt, Eur.Phys.J. **C63** (2009) 189–285, arXiv:0901.0002 [hep-ph].

[26] A. Bialas, M. Bleszynski, and W. Czyz, Nucl. Phys. **B111** (1976) 461.

[27] P. Steinberg, arXiv:0703002 [nucl-ex].

[28] J. Pumplin et al., JHEP **0207** (2002) 012, arXiv:0201195 [hep-ph].

[29] GEANT4 Collaboration, S. Agostinelli, et al., Nucl. Instrum. Meth. **A506** (2003) 250–303.

[30] ATLAS Collaboration, Eur. Phys. J. **C70** (2010) 823–874.

[31] ATLAS Collaboration, Phys. Lett. **B719** (2013) 220–241.

[32] ATLAS Collaboration, Phys. Rev. Lett. **111** (2013) 152301.

[33] ATLAS Collaboration, Eur. Phys. J. **C73** (2013) 2304, arXiv:1112.6426 [hep-ex].

[34] ATLAS Collaboration, Eur. Phys. J. **C73** (2013) 2509, arXiv:1304.4739 [hep-ex].

[35] ATLAS Collaboration, Phys. Rev. **D86** (2012) 014022, arXiv:1112.6297 [hep-ex].

[36] ATLAS Collaboration, Eur. Phys. J. **C73** (2013) 2306, arXiv:1210.6210 [hep-ex].

[37] S. van der Meer, Tech. Rep. CERN-ISR-PO-68-31. ISR-PO-68-31, CERN, Geneva, 1968.

[38] ATLAS Collaboration, Eur. Phys. J. **C71** (2011) 1630, arXiv:1101.2185 [hep-ex].

[39] M. Alvioli and M. Strikman, Phys. Lett. **B722** (2013) 347–354, arXiv:1301.0728 [hep-ph].

[40] M. Alvioli, L. Frankfurt, V. Guzey, and M. Strikman, arXiv:1402.2868 [hep-ph].

[41] C. E. Coleman-Smith and B. Müller, Phys. Rev. **D89** (2014) 025019, arXiv:1307.5911 [hep-ph].